Interference Model for an Array of Wave-Energy-Absorbing Flexible Structures

C. Nové-Josserand,* R. Godoy-Diana, and B. Thiria
Laboratoire de Physique et Mécanique des Milieux hétérogènes (PMMH UMR 7636), ESPCI Paris, PSL Research University, Sorbonne Université, Université Paris Diderot, 10 rue Vauquelin, 75005 Paris, France

(Received 18 May 2018; revised manuscript received 23 October 2018; published 21 March 2019)

Considerable work has been undertaken for the improvement of wave-energy converters and array design. It has recently been suggested that by extracting wave energy, these farms could also serve to protect shorelines from wave damage. The present work focuses on the local effects of wave-structure interactions within an array of oscillating absorbers to optimize global effects, such as reflection, damping, and energy absorption. We use a model system of flexible blades, subjected to monochromatic waves, and develop a simplified one-dimensional model to predict optimal configurations, depending on various parameters, which include the number of blades, their spacing, and their flexibility. Optimal configurations are found to be close to regular patterns, and the impact of array configurations is shown to be limited regarding wave dissipation, mainly due to a competition between reflection and absorption.

DOI: 10.1103/PhysRevApplied.11.034054

I. INTRODUCTION

Ocean waves have large potential for renewable energy that could reach 2 TW [1]. Yet only a small portion is currently harvested, and mostly through early-stage prototypes [2]. Additionally, when this energy is not harvested, it is transmitted to the shoreline, where it can cause coastal erosion. Absorbing the energy of waves through converters therefore presents a double advantage.

Great effort has been made in the last two decades regarding the development of wave-energy converters (WEC), with many proposed designs (see Refs. [3,4] for reviews). These devices are nonetheless limited in power output and efficiency and, thus, deployments in large arrays will be necessary. Each device can then be impacted by the presence of neighbors, due to wave interference.

Many studies have explored the influence of array configurations on WEC performance and have highlighted the possible strong interference between waves within the array [5–10]. One interesting phenomenon is observed when the devices are placed in regular patterns, separated by a distance equal to half the wavelength of the incoming wave. In this case, strong reflection is observed, similar to the Bragg resonance seen in wave scattering through crystal lattices [11]. This strong effect has been the source of extensive research in areas of solid-state physics and acoustics, with specific interest for the development of metamaterials that could absorb waves efficiently [12–16]. This research can also be extended to water waves [17] and could apply to WEC-farm design. Indeed, these arrays could also serve to dampen waves and reduce coastal erosion since their aim is to extract the energy of waves over large surface areas [18–20]. In this sense, Bragg resonance could be very useful. Yet, while the associated array configuration could benefit wave damping, it is also found to reduce the device oscillations, thereby limiting power extraction. This was observed experimentally by Nové-Josserand *et al.* [21] and numerically by Garnaud and Mei [22]. The latter developed an analytical model describing the interaction of waves and an array of small wave-energy-converting buoys. Band gaps (i.e., the range of frequencies over which wave propagation is prohibited) and array power absorption were predicted with use of the Froude-Krylov approximation to model the force on a WEC element and multiple-scale analysis. The results demonstrated a strong reduction of the array's efficiency in the case of Bragg resonance. Similarly, Renzi and Dias [23] studied the effect of the lateral spacing of flap-type converters on the resulting capture factors. Very clear peaks in performance were found. These observations highlight the difficulty in designing optimal wave farms, which will have to result from a trade-off between wave damping and energy harvesting.

Array optimization has been studied in a number of numerical studies, based on various applied-mathematical tools. A semianalytical model was, for example, recently developed by Göteman *et al.* [24] to test configurations that minimize power fluctuations. However, most optimization studies thus far have been limited to small arrays or to specific conditions, as these often require extensive numerical calculations. It is therefore difficult to obtain general conclusions.

*clotilde.nove-josserand@espci.fr

In this paper, we develop a simple one-dimensional (1D) interference model to evaluate the benefit of optimal array configurations in terms of both wave-energy absorption and damping. Following an experimental validation using a small-scale array of flexible blades, both regular and irregular arrays are considered and the influence of local scattering coefficients of each individual item on the global performances of the entire array is discussed.

II. METHODS

A. Theoretical model

On the basis of the small-scale experiments presented in Ref. [21], we study the interaction between planar monochromatic waves and an array of partially submerged slender, flexible blades. Each row within the array is composed of an infinite number of elastic structures ("blades"). As these bend under the action of the incoming fluid, part of the incoming-wave energy is dissipated through the associated internal work of the material, and the rest is either reflected or transmitted downstream. This system of multiple infinite rows can therefore be modeled as a 1D system, in which each row represents a single unit of the full array. The energy dissipated through each row is then evaluated experimentally along with that associated with the reflected and transmitted waves, thus providing information on the global energy distribution within the system (see Fig. 1).

1. Scaling

Each flexible blade within the array is subjected to both inertial and viscous forces due to its interaction with water waves. This is expressed as

$$\sum \mathbf{F}_{\text{ext}} = \mathbf{F}_{\text{viscous}} + \mathbf{F}_{\text{inertia}} = \mathbf{F}_{\text{viscous}} + \iint_S p\,\hat{\mathbf{n}}\,dS, \quad (1)$$

where p is the pressure due to the fluid acting on the wetted surface S in the normal $\hat{\mathbf{n}}$ direction. Assuming potential flow and linear waves, the pressure term is further expressed as

$$p = \iint_S -\rho\left(\frac{\partial \Phi}{\partial t} + gz\right)\hat{\mathbf{n}}\,dS, \quad (2)$$

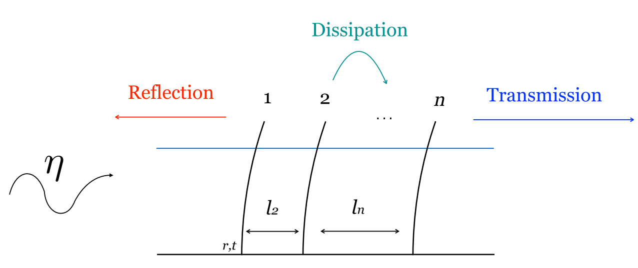

FIG. 1. The 1D model.

$$\Phi = \Phi_I + \Phi_D + \Phi_R, \quad (3)$$

where Φ is the total wave potential such that fluid velocity can be written $\mathbf{u} = \nabla\Phi$, which includes an incident term Φ_I, a diffracted term Φ_D, and a radiated term Φ_R. Total inertial forces are therefore shared between hydrodynamic forces in the incident waves (Froude-Krylov force) and hydrodynamic forces due to the structure disturbing the waves (diffraction and radiation forces).

The importance of each force term can be evaluated with two dimensionless numbers: the Keulegan-Carpenter number $= uT/D$, which compares viscous terms with inertial terms, and the diffraction number $\mathcal{D} = D/\lambda$, which divides the size of the object by the wavelength. Note that $u = |\mathbf{u}|$ is the orbital velocity of the fluid particles, T is the wave period, D is the characteristic size of the object, and λ is the wavelength.

Flap-type wave-energy converters can be described as line absorbers and rely on inertially driven forces. Therefore, they are generally associated with low Keulegan-Carpenter numbers and tend to be wide objects to maximize their capture width and efficiency. Diffraction thus plays an important role in the array forces.

2. Interference model

Let $\eta = \text{Re}\{ae^{i(kx-\omega t)}\}$ be the incident complex waveform with amplitude a, wave number k, and angular frequency ω. As this wave travels through the array, it will interact with each row n of an infinite number of blades, which behaves as a single item transmitting part of the incident wave with a local coefficient t and reflecting another part with a local coefficient r (see Fig. 1).

In the 1D case, each row is subjected to the sum of forces induced by waves traveling in the two opposing directions. We take incident and transmitted (η_t) waves traveling in the positive x direction and reflected waves (η_r) traveling in the negative x direction. The associated horizontal wave-particle motions are illustrated in Figs. 2(a) and 2(b).

Two waves traveling in opposite directions force water particles to move in opposite elliptic trajectories. Taking the transmitted wave $\eta_t = \text{Re}\{tae^{i(kx-\omega t)}\}$ and reflected wave $\eta_r = \text{Re}\{rae^{i(kx+\omega t)}\}$, we can write the corresponding dynamic excitation forces as

$$\mathbf{F}_t = M\dot{\mathbf{u}}_t = F_t\hat{\mathbf{e}}_x, \quad (4)$$

$$\mathbf{F}_r = M\dot{\mathbf{u}}_r = F_r(-\hat{\mathbf{e}}_x), \quad (5)$$

where M is the mass of the displaced fluid, $\dot{\mathbf{u}}_t$ and $\dot{\mathbf{u}}_r$ are the orbital accelerations of the fluid particles, associated with transmitted and reflected waves, respectively, and $\hat{\mathbf{e}}_x$ is the unit vector in the positive x direction [see Fig. 2(c)]. Only small deformations are assumed here. Given that for constant water depth, wave frequency, and wave number,

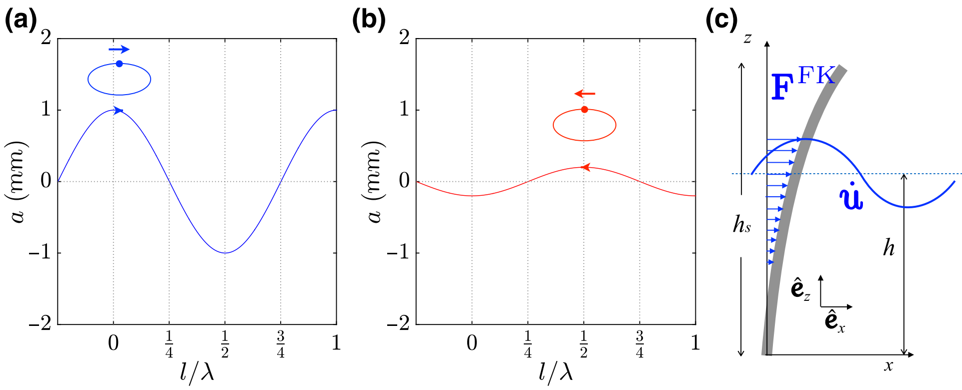

FIG. 2. (a) Incident (or transmitted) and (b) reflected waves with associated horizontal wave-particle motion x. (c) The distributed Froude-Krylov wave force $\mathbf{F}^{\mathrm{FK}}$ associated with the incident wave on a partially submerged flexible blade.

$\dot{u} = |\dot{\mathbf{u}}|$ is proportional to the wave amplitude a, the total excitation force $\mathbf{F}_{\mathrm{tot}}$ acting on the front row becomes

$$\mathbf{F}_{\mathrm{tot}} = \sum \underline{F} = \mathbf{F}_t + \mathbf{F}_r = \mathcal{A} \cdot \mathbf{F}^{\mathrm{FK}}, \tag{6}$$

where $\mathcal{A}$ is an amplification factor of the dynamic Froude-Krylov force $\mathbf{F}^{\mathrm{FK}} = M\dot{\mathbf{u}}_i$ associated with the incident wave, resulting from array interference.

In the more-general case, any row n of an array composed of N rows will be subjected to the total wave force F_n resulting from interfering transmitted (incident in the case of the front row) and reflected waves from the array:

$$\mathbf{F}_n = \mathcal{A}_n \mathbf{F}^{\mathrm{FK}}, \tag{7}$$

$$\mathcal{A}_n = |T_n - R_n|. \tag{8}$$

The resulting coefficients R_n and T_n are obtained, as follows, from the sums of geometric series:

$$R_n = \underbrace{\frac{rt^n e^{i\sum_{m=1}^{n}\varphi_m}}{1 - r^2 e^{i2\varphi_{(n+1)}}}}_{\text{immediate neighbors}} \underbrace{\sum_{k=0}^{N-n-1} t^{2k} e^{i2\sum_{m=n+1}^{n+k+1}\varphi_m}}_{\text{subsequent rows}},$$
$$T_n = \frac{t^{(n-1)} e^{i\sum_{m=1}^{n}\varphi_m}}{1 - r^2 e^{i2\varphi_n}}, \tag{9}$$

where $\varphi_n = l_n 2\pi/\lambda$ corresponds to the phase shift of incident transmitted waves η_{tn} at row n with respect to the incident wave η.

The global force-amplification factor resulting from array wave interference can therefore be predicted with Eq. (8) and provides an indication of the local excitation force applied on each row. In the following sections, we derive expressions for the global internal dissipation (K_a), reflection ($\mathcal{R}$), and transmission ($\mathcal{T}$) coefficients arising from this interference model.

3. Energy dissipation K_a

At the local scale of a single row, the energy associated with the incident wave is shared between a reflected part of ratio r^2, a transmitted part of ratio t^2, and a dissipated part of ratio $d = 1 - (r^2 + t^2)$. The dissipated energy depends on the device oscillations and includes terms for both internal dissipation (k_a) due to the device's restoring force (internal friction or power take-off damping) and external dissipation (k_d) due to the added friction losses caused by the presence of the fluid (drag).

The device is modeled as a cantilevered flexible beam [see Fig. 3(c)] bending on its first mode of deformation, for which the motion is described by that of a damped oscillator. Assuming small oscillations, linear-beam theory applies, suggesting that the local position of the blade $x(z,t)$ is a function of the maximal blade-tip deflection $\mathbf{X}(t)$ and is proportional to the total beam loading and the elastic restoring force:

$$x(z,t) = \mathbf{v}_1(z) \cdot \mathbf{X}(t). \tag{10}$$

$v_1(z)$ is the mode shape and is expressed as follows:

$$v_1(z) = \frac{1}{2}\Bigg[\cos k_1 z - \cosh k_1 z + \left(\frac{\sin k_1 h_s - \sinh k_1 h_s}{\cos k_1 h_s + \cosh k_1 h_s}\right)(\sin k_1 z - \sinh k_1 z)\Bigg], \tag{11}$$

where h_s is the total length of the blade and k_1 is the first root of the characteristic equation in vacuum. As described in Ref. [21], the power associated with internal and external dissipation can be written as

$$\mathcal{P} = 2[\Gamma_{\mathrm{int}}(m + m_a)\dot{x}^2] + \frac{1}{2}\rho_w C_D A u_r^3, \tag{12}$$

$$u_r(z) = u_a(z) - \dot{x}(z), \tag{13}$$

$$u_a(z) = a\omega \frac{\cosh k(h+z)}{\cosh kh}, \tag{14}$$

where Γ_{int} is the damping coefficient related to the internal work of the oscillator, m and m_a are, respectively, the mass of the beam and the added mass of the fluid

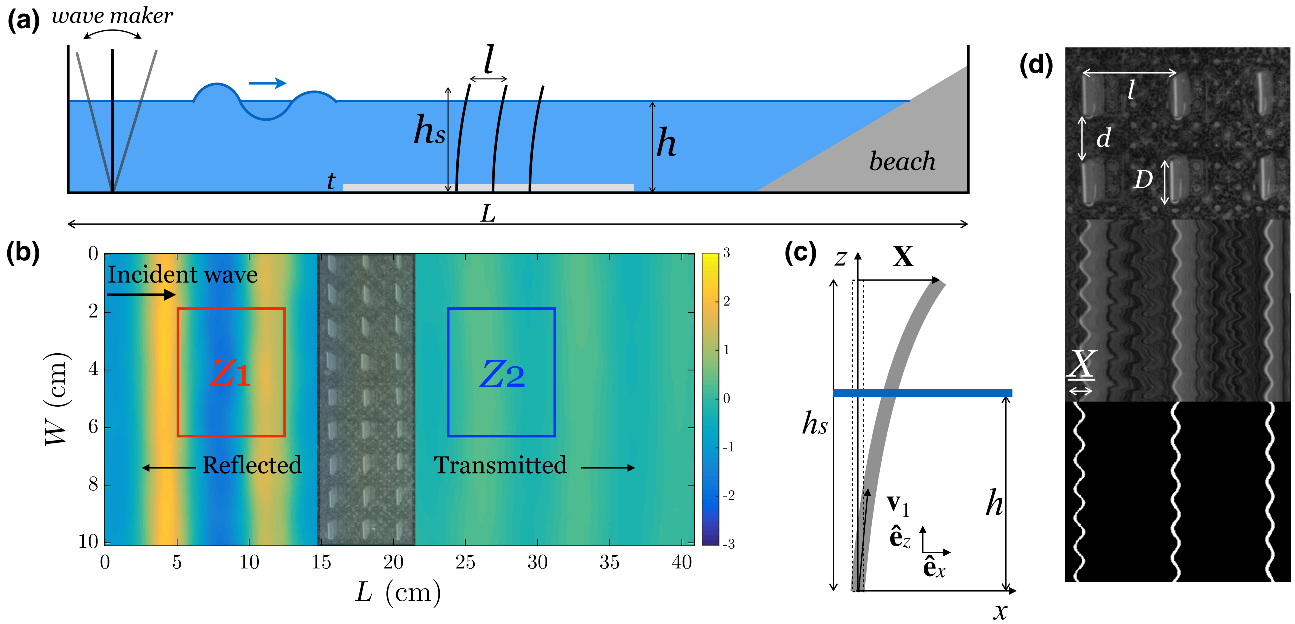

FIG. 3. (a) The experimental setup. (b) Example of a typical treated surface-wave map before and after the blades, with selected zones of analysis Z1 (red) and Z2 (blue) for $\mathcal{R}$ and $\mathcal{T}$ measurements. (c) The cantilever-beam model. (d) Characteristic parameters of blades (top) and spatiotemporal plots (bottom) used for blade-tip tracking analysis (see Ref. [21] for the detailed method description).

displaced by the submerged part of the beam, C_D is an empirical drag coefficient taken equal to 2 for a plate shape, A is the projected surface subjected to incoming flow, and u_r is the relative velocity of the blade and the fluid particles. For any given beam geometry and mechanical properties, and any imposed wave conditions, the dissipated power is therefore proportional to the oscillation amplitudes squared. The oscillation amplitude itself depends on the wave amplitude, so $\dot{x}$ varies together with X. The power of the incoming waves per unit area is given by $P_w = \frac{1}{2}\rho g a^2 v_g$, where v_g is the group velocity of the wave, and is related to the phase velocity through $v_g = (v_p/2)(1 + 2kh/\sinh 2kh)$. The internal dissipation is given by the ratio of the internal damping energy:

$$k_a = \frac{P}{P_w} = \frac{\Gamma_{\text{int}}(m + m_a)\dot{x}^2}{\frac{1}{2}\rho g a^2 v_g}. \tag{15}$$

From Eqs. (10) and (15), one can easily see that $k_a \propto \dot{x}^2 \propto X^2$. Therefore, the global absorption factor will also depend on the amplification factor as follows:

$$k_a(X^2) = 1 - (r^2 + t^2 + k_d), \tag{16}$$

$$K_a = \sum_{n=1}^{N} \mathcal{A}_n^2 k_a. \tag{17}$$

Using the amplification-factor model, we predict the maximal potential-energy dissipation using Eq. (17) based on the array layout.

To highlight the effect of array interference on the global absorption coefficient K_a, the results are compared with a theoretical reference coefficient $K_{a_{\text{ref}}}$, which we define as the sum of nonamplified individual dissipation coefficients, taking into account only cumulative reduced transmission throughout the array. This is expressed as

$$K_{a_{\text{ref}}} = \sum_{n=0}^{N-1} t^{2n} k_a = k_a \frac{1 - t^{2N}}{1 - t^2}. \tag{18}$$

The transmission coefficient is squared since the dissipation coefficient is a function of X^2 [see Eqs. (10) and (15)].

4. Global reflection $\mathcal{R}$

Following similar interference principles, we use the same method to predict the total global reflection coefficient of the array $\mathcal{R}$. In this case, the sum of all reflected waves is considered at position x_1^+ in front of the first row. Taking only first-order reflections from subsequent rows, we have

$$\eta_R = \eta_{r1} + \eta_{r2} + \eta_{r3} + \cdots + \eta_{rn} = \sum_{n=1}^{N} \eta_{rn}. \tag{19}$$

Each row n reflects a wave η_{rn} with a phase shift $\varphi_n = l_n 2\pi/\lambda$ due to the distance l_n separating two neighboring rows. If we first consider a simple case where the distance l_n between each row is the same constant l, then the sum of all reflected waves can be written as a power series [Eq. (20)]:

$$\eta_R = \mathrm{Re}\{ae^{i(kx)}R_z\}, \tag{20}$$

where $R_z = [r(1-(t^2e^{i(2\varphi)})^N]/(1-t^2e^{i(2\varphi)})$. The total reflection coefficient $\mathcal{R} = |R_z|$ can therefore be calculated for any given phase shift φ. The theoretical case without array effects gives $\mathcal{R}_{\mathrm{ref}} = r(1-t)^{2N}/(1-t)^2$, which coincides with Bragg scattering ($\varphi = 0$).

If we consider independently varying values of l_n through the array, Eqs. (9) and (20) lead to the following expression for the global reflection coefficient $\mathcal{R}$ of the entire array:

$$\mathcal{R} = r\sum_{k=0}^{N-1} t^{2k}e^{i2\sum_{m=1}^{k+1}\varphi_m}. \tag{21}$$

5. Global transmission $\mathcal{T}$

Without any array effects, the global transmission coefficient would simply be expressed as $\mathcal{T}_{\mathrm{ref}} = t^N$, where N is the total number of rows and t is the local transmission coefficient of a single row. However, array layout affects wave interference, which, on the basis of a similar reasoning, leads to the following expression for the global transmission coefficient at position x_N^+ just behind the last row of the array:

$$\mathcal{T} = \frac{t^N e^{i\sum_{m=1}^{N}\varphi_m}}{1-r^2e^{i2\varphi_N}}. \tag{22}$$

On the basis of local coefficients r and t, it therefore possible to evaluate the total energy distribution in our system using global dissipation (K_a) [Eq. (17)], reflection ($\mathcal{R}$) [Eq. (21)], and transmission ($\mathcal{T}$) [Eq. (22)] coefficients for any given separating distances l_n.

B. Experimental validation

To validate the model, small-scale experiments are performed with an array of flexible, slender blades subjected to a surface-water-wave field created in a wave canal 0.6 m wide and 1.8 m long. A flapping-type wave maker is used to create controlled monochromatic waves and an angled polymer (PVC) sheet is placed at the end of the canal to act as a beach and minimize wall reflections. A sketch of the experimental setup is presented in Fig. 3(a). The blades are made from Mylar® of thickness 350 μm, density 1380 kg/m^3 and Young's modulus (E) 5 GPa. Individual Mylar blades are fixed to Lego® blocks, which are arranged on a Lego base board, thus allowing easy configuration variations. Experiments are performed at the natural resonant frequency f_0 of the blades, measured to be 5 Hz in water. The blades are 9 cm long (h_s), fixed to a Lego block of 1-cm height and a base of 5-mm thickness. The water depth is chosen to match deep-water conditions, and is kept at 8 cm, thus giving a submergence ratio h/h_s of =0.83 [see Fig. 3(c)]. The lateral spacing d between neighboring blades is fixed at $\lambda/2$ (equal to four Lego spaces of 8 mm each). Wave and blade characteristics are summarized in Tables I and II, respectively.

TABLE I. Wave characteristics: frequency f, and amplitude a, wavelength λ of imposed waves, and depth h of water.

f (Hz)	a (mm)	λ (cm)	h (cm)
5	0.7	7.16	8

In these conditions, the Keulegan-Carpenter number is $\mathcal{O}(10^{-1})$, and the diffraction number D/λ is around 0.2, suggesting that inertial forces are dominating and array diffraction is not negligible. Our model therefore applies.

Two sets of experiments are performed:

(a) The number of rows N is set to 2 and the longitudinal spacing l_2 between row 1 and row 2 is varied over the range $[\lambda/4;\lambda]$.

(b) The number of rows N is set to 3 and the longitudinal spacing l_3 between row 2 and row 3 is varied over the range $[\frac{\lambda}{4};\lambda]$. Spacing l_2 between row 1 and row 2 is fixed at $\lambda/4$.

For each configuration, 400 images are recorded with a Phantom V9 camera at a recording frequency of 200 fps, therefore covering ten wave periods. To avoid strong lateral reflections and canal modes, recordings are started when the first waves have traveled through the camera field. The surface-wave maps are treated by the synthetic schlieren method [25]. A transparent Lego base and transparent Lego blocks are used to benefit from this method over the entire image. Global reflection (K_r) and transmission (K_t) coefficients are then calculated from these treated surface-wave maps with use of two separate zones of analysis before (Z1) and after (Z2) the array [see Fig. 3(b)]. It is assumed that the transverse average of the waves in each zone takes the form

$$\eta(x) = \begin{cases} ae^{-ikx} + \mathcal{R}ae^{ikx} & \text{in Z1,} \\ \mathcal{T}ae^{-ikx} & \text{in Z2.} \end{cases} \tag{23}$$

Taking x_a and x_b $\in Z1$, and $x_c \in Z2$, we can define the reflection ($\mathcal{R}$) and transmission ($\mathcal{T}$) coefficients as

$$\mathcal{R} = \frac{e^{-ikx_b} - H_1e^{ikx_a}}{H_1e^{ikx_a} - e^{ikx_b}}, \tag{24}$$

TABLE II. Blade characteristics: length h_s, width D, thickness e, Young's modulus E, and density ρ of blades.

h_s (cm)	D (cm)	e (μm)	E (GPa)	ρ (kg/m^3)
9	1.4	350	5	1380

$$\mathcal{T} = \frac{e^{-ikx_a} + \mathcal{R}e^{ikx_a}}{H_2 e^{-ikx_c}}, \tag{25}$$

where H_1 and H_2 are transfer functions defined as $\eta(x_b)/\eta(x_a)$ and $\eta(x_a)/\eta(x_c)$, respectively. All three points x_a, x_b, x_c are selected randomly and the final coefficients are averaged over 200 iterations.

Finally, the calculated transmission coefficient $\mathcal{T}$ of each configuration is normalized by that calculated for a reference case without blades $\mathcal{T}_0$ (giving $\tilde{\mathcal{T}}$) to separate array damping from natural wave dissipation. A reference case (without blades but with the base board) is therefore taken at the end of each set of experiments. These coefficients are calculated over the central area of the tank, where imposed waves are linear and monochromatic, thus justifying transverse averaging. The results obtained for a single row are $\mathcal{R} \approx 0.3$ and $\tilde{\mathcal{T}} \approx 0.7$. These coefficients are those used for local r and t value inputs in the model. Because of the difficulties in avoiding beach and motor reflections, the measured reflection coefficient is not that representative of blade reflections only. Therefore, when calculating the global absorption (K_a) and transmission ($\mathcal{T}$) coefficients, we replace local r by that due to the presence of blades only, measured as $r_{\text{blades}} = r - r_{\text{ref}}$, where r_{ref} corresponds to the coefficient measured without blades (approximately 0.1). Results are presented in Figs. 4(a) and 4(c).

The second part of the analysis focuses on the bending of the blades, which relies on the recording of the beam movements. The top of each blade is highlighted with white tape to contrast with the dark dotted pattern used for the schlieren method. The movement of each blade end is quantified by a spatiotemporal stacking method as provided by the software package ImageJ [see Fig. 3(d)]. We can therefore compare normalized blade oscillations $\tilde{X}$ for each row with normalized wave forcing $\tilde{F}^{\text{FK}}$ for each row. This is represented by the amplification factor $\mathcal{A}$ for both quantities. Results are presented in Figs. 4(b) and 4(d). The experimental results are plotted against l/λ, where λ is found to vary between 0.065 and 0.07. This may lead to a slight shift of the curves.

The results show good agreement between experimental data and model predictions, especially regarding blade-oscillation amplification factors $\mathcal{A}$, with clear peaks and

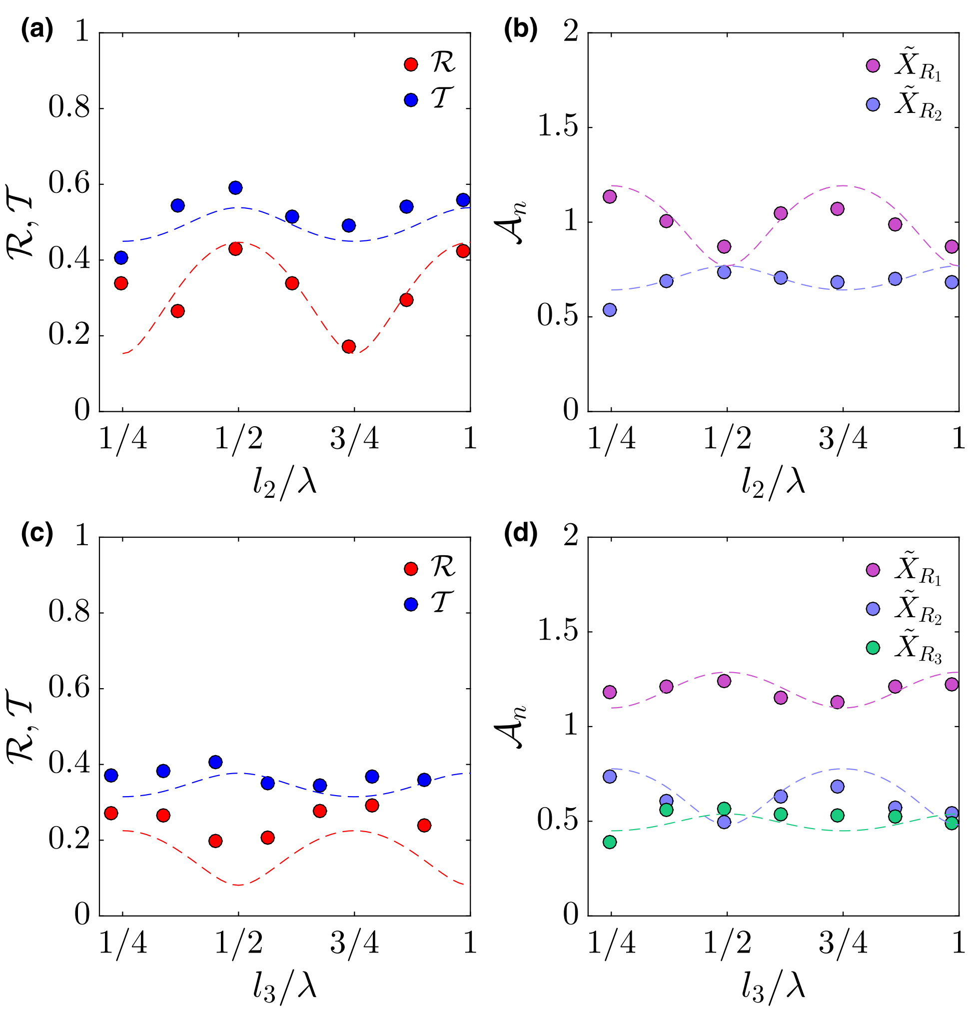

FIG. 4. Measured global reflection ($\mathcal{R}$) and transmission ($\mathcal{T}$) coefficients (dots) for an array composed of two rows (a) and three rows (c) compared with numerical values calculated from Eqs. (21) and (22) (dotted lines). Normalized blade oscillations $\tilde{X}$ (dots) for each row R_n of an array composed of two rows (b) and three rows (d) compared with numerical values of $\mathcal{A}_n$ calculated from Eq. (8) (dotted lines). Spacings l_2 in the case of $N = 2$ and l_3 in the case of $N = 3$ are varied within $[\lambda/4; \lambda]$.

troughs at $l = \lambda/4$ and $l = \lambda/2$, as expected. The results regarding global reflection and transmission coefficients are not as good in the case of $N = 3$. This could be due to the experimental uncertainties for local r and t calculations. The qualitative variations are nonetheless coherent.

III. RESULTS AND DISCUSSION

We now use the model described above to explore all possible array configurations to evaluate their influence on blade oscillations and wave damping.

A. Regular configurations

We first compare two bounding cases for regular configuration patterns (i.e., arrays with constant spacing l between rows), which correspond to spacing ratios $l = \lambda/2$ and $l = \lambda/4$. Taking the same local coefficients as those measured experimentally ($r = 0.2$, $t = 0.7$, $d = 0.4$), we explore the effect of increasing the number of rows in the array by examining the amplification factors calculated from Eq. (8) (see Fig. 5). The results are compared with reference case without amplifications (i.e., assuming a series of single independent rows). These are represented by asterisks in Fig. 5 and are calculated as t^{n-1} for each row n.

As expected, these results show the strong influence of the arrangement on front-row oscillations, with a 30% decrease in values for $l = \lambda/2$ versus a 10% increase for $l = \lambda/4$, and these effects hold true throughout the array, with similar attenuated effects for each subsequent row.

The global reflection and transmission coefficients are also compared in Fig. 6, with use of Eqs. (21) and (22). Here again, a reference case is plotted in asterisks to identify the effect of array amplifications on $\mathcal{T}$ (note that the results for $\mathcal{T}$ would match exactly those for $l = \lambda/2$, as described in Sec. II 4). As previously seen for amplification factors, a clear difference is noticed, especially regarding the reflection coefficients, with a maximum difference of around 25% obtained for arrays of ten rows.

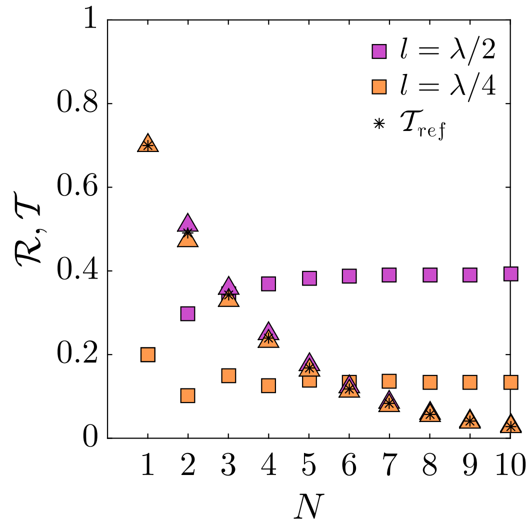

FIG. 6. Predicted global reflection ($\mathcal{R}$) (squares) and transmission ($\mathcal{T}$) (triangles) coefficients as a function of array size (increasing number of rows N). Results for constant array spacings $l = \lambda/2$ and $l = \lambda/4$ are presented in red and orange, respectively. Results are compared to the reference case without amplification effects ($\mathcal{T}_{\mathrm{ref}}$).

The transmission coefficients, on the other hand, fall on very similar curves, and do not deviate beyond 15% from the reference case ($N = 5$). This suggests a competition between reflection and absorption, with a maximal gain in absorption when reflection is minimal, whereas transmission is little affected and depends mainly on array size. Another noticeable difference concerns the change in variations for increasing array sizes. While $\mathcal{R}$ increases steadily with N for $l = \lambda/2$ before reaching a limit at $N = 5$, it decreases very slightly and in oscillatory form for $l = \lambda/4$. A similar observation can be made regarding amplification factors, with mirrored trends (see Fig. 5). This oscillation is thought to come from a pairing effect of amplifications, with mimima observed for even arrays and maxima observed for odd arrays.

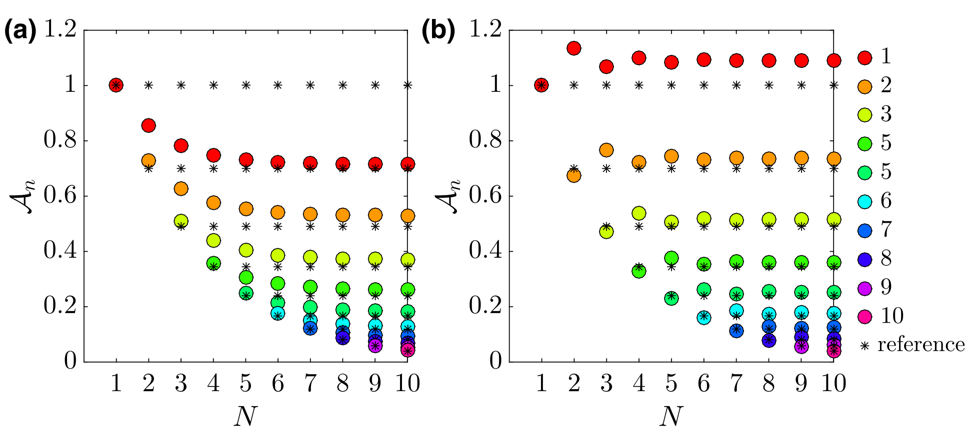

FIG. 5. Predicted amplification factors $\mathcal{A}_n$ for each row n of the array as a function of increasing total number of rows N. Results for constant array spacing $l = \lambda/2$ (a) and constant array spacing $l = \lambda/4$ (b). Theoretical oscillation factors without amplification (reference) are presented as asterisks.

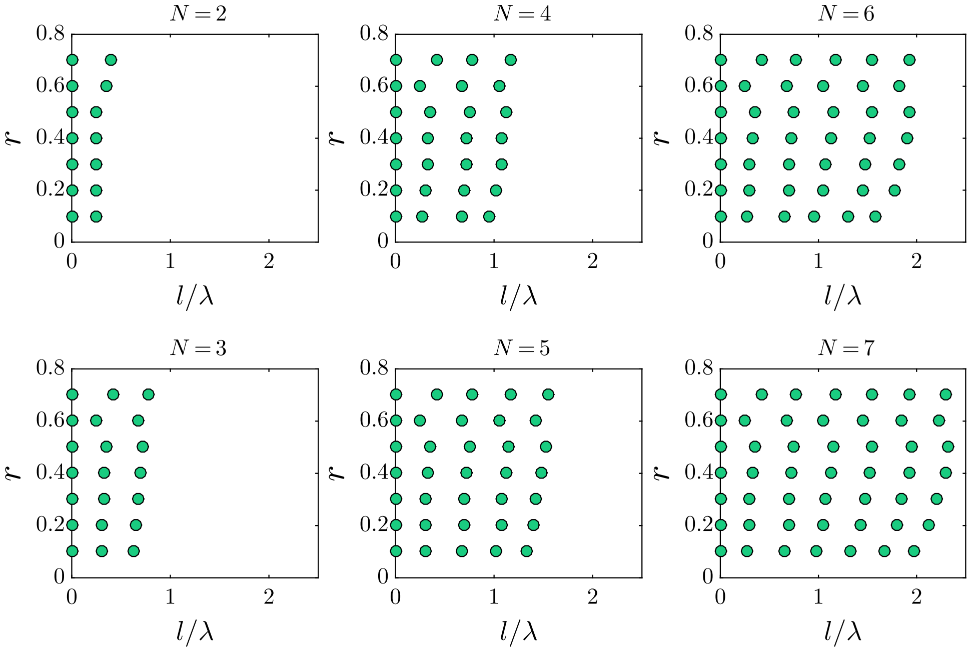

FIG. 7. Optimal configurations as a function of $\{r;t\}$ values for increasing array size from $N=2$ to $N=7$. The local dissipation value d is fixed at 0.4.

B. Optimal configuration

It is clear that variations of $\mathcal{A}_n$, $\mathcal{R}$, and $\mathcal{T}$ depend on the input parameters r and t, which are so far measured from experimental data. If these coefficients now become changeable, for example, via a modification of the confinement ratio, or blade flexibility and shape, then these tendencies will be altered. Additionally, given that $\lambda/2 = 2\times\lambda/4$, the benefits of $l=\lambda/4$ are diminished

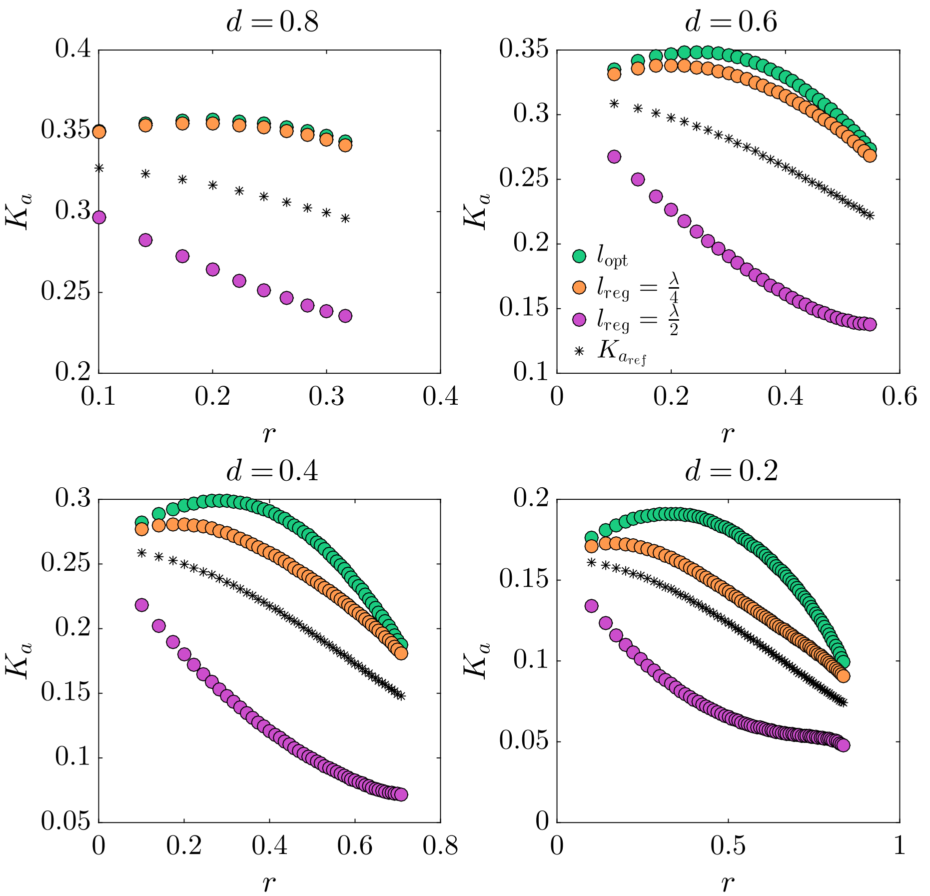

FIG. 8. Variations of global dissipation coefficient K_a depending on local d and $\{r,t\}$ values for an array composed of three rows. Results for the optimal configuration and regular configurations are compared with the reference values without any array effects ($K_{a_{\mathrm{ref}}}$).

by the negative impact of $l = \lambda/2$ spacings on blade oscillations for arrays with $N > 2$. This suggests that for larger arrays, configurations causing maximal oscillation amplifications may be irregular, whereby the spacing between rows is no longer constant. These optimal configurations are determined by our scanning all possible combinations of l_n spacings and calculating their associated amplification factors $\mathcal{A}_n$. The optimal array is that providing the maximal global amplification factor $\mathcal{A}_{\text{tot}} = \Sigma \mathcal{A}_n$. Resulting configurations are presented in Fig. 7 for arrays ranging from two to seven rows and for varied local coefficients r with a fixed local dissipation coefficient $d = 0.4$ (taken from experimental data). In our experimental case, internal dissipation k_a accounts for approximately one third of the total dissipation d. In Sec. III B, we therefore choose to arbitrarily vary our local coefficients on the basis of the local energy-balance condition: $r^2 + t^2 + d = 1$, with $k_a = d/3$.

As expected, optimal configurations deviate from regular arrays for all sizes $N > 2$. While the observed patterns are not yet understood, these variations are thought to stem from the local nature of the amplification effects. Given that r and t are of $\mathcal{O}(10^{-1})$, interference will have an impact only on neighboring rows. This would explain why both even and odd arrays may transition through semiregular configurations composed of combined pairs of rows.

The benefit of the determined optimal configurations is further evaluated and the associated global dissipation coefficients are compared with those of the regular bounding cases, along with the reference case (asterisks), as described in Eq. (18). Results are plotted in Fig. 8 for an array of three rows, for varied local dissipation coefficient $d \in [0.1 - 0.8]$. These plots clearly show the negative impact of regular arrays $l = \lambda/2$ as opposed to the benefit of both regular arrays $l = \lambda/4$ and optimal arrays on global wave absorption, with deviations of up to $\pm 50\%$ ($d = 0.2$). However, the difference between the optimal configurations and the regular array $l = \lambda/4$ reduces as dissipation increases, and becomes negligible when $d = 0.8$. More globally, larger amplifications are found for lower values of d and when $r \times t$ is maximum; the greater the transmitted energy, the larger the impact of subsequent interference.

Figure 9 compares the reflection and transmission coefficients of all three configurations, along with the reference $\mathcal{T}_{\text{ref}}$, as a function of r and d. Once again, the results demonstrate a clear difference between the two regular

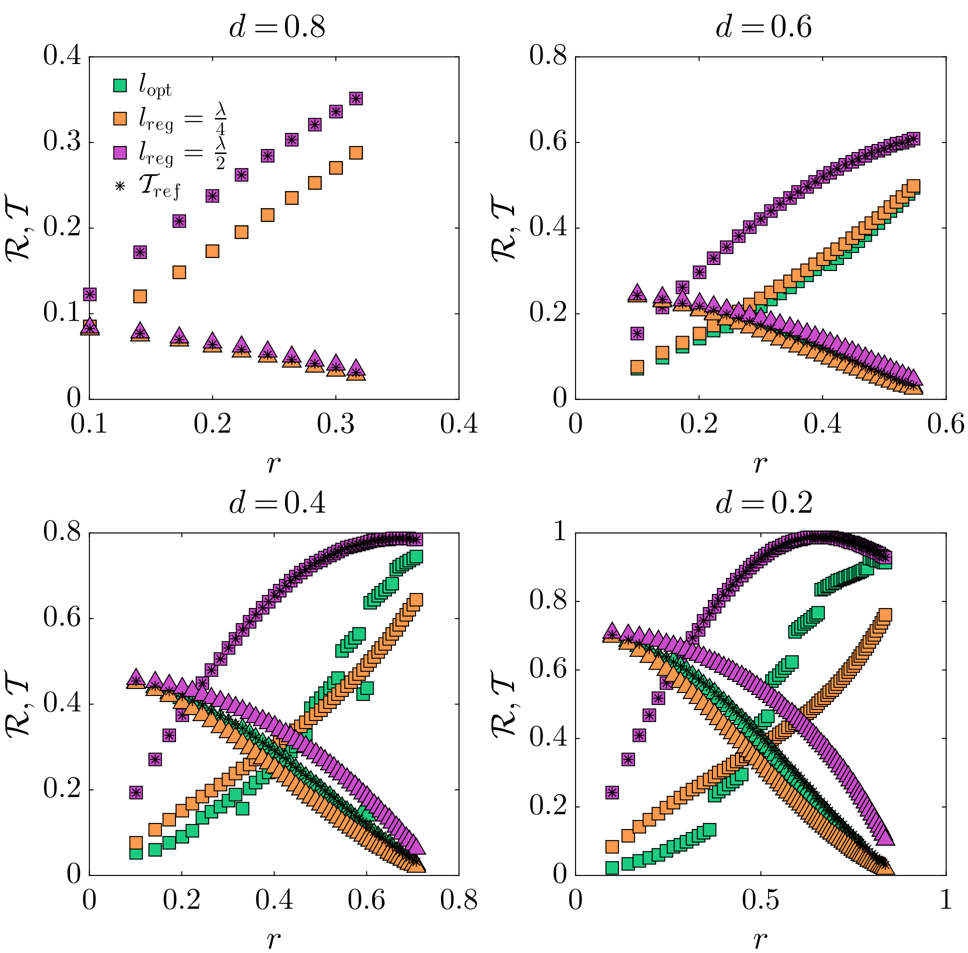

FIG. 9. Variations of global reflection ($\mathcal{R}$) (squares) and transmission ($\mathcal{T}$) (triangles) coefficients depending on local d and r, t values for an array composed of three rows. Reference transmission coefficients $\mathcal{T}_{\text{ref}}$ are plotted in black for comparison.

arrays, with overall higher reflection and transmission when $l = \lambda/2$, in particular for the lowest values of d, for which a reduction of 60% can be obtained. As noticed for blade oscillations, the deviations between results obtained for optimal configurations compared with regular arrays $l = \lambda/4$ depend strongly on the values of d. The curves match almost perfectly in the low range of d, while in the higher range, the reflection values for optimal configurations strongly deviate from the regular $l = \lambda/4$ case. This is because interference play a larger role as more energy is transmitted through the successive rows. The differences calculated are to 50% (when $d = 0.2$ and $r = 0.4$). Furthermore, these deviations vary with an inflection point located around $r = 0.5$ beyond which optimal configurations provide larger reflections. This corresponds to the point at which optimal configurations demonstrate a shift in pattern (see Fig. 7). Finally, all results converge toward similar values of $\mathcal{R}$ and $\mathcal{T}$ when r coefficients are the largest. In that case, the energy transferred is almost nil and the effect of subsequent rows becomes negligible, so the performance of all three configurations relies mostly on the performance of the front row only. Similar results are found for the larger arrays.

IV. CONCLUSION

Following previous observations made regarding the influence of array configurations on wave-absorber oscillations, we present a simple one-dimensional model able to predict the effects of wave interference on array performance. On the basis of known local reflection and transmission coefficients of an isolated row, this model is used to explore optimal array configurations regarding wave-energy damping and absorption. The results confirm the previous experimental data by showing that in regular arrays a separating distance $l = \lambda/2$ leads to a very large global reflection coefficient, but reduces blade oscillations, while the contrary is found for a separating distance $l = \lambda/4$. Optimal configurations regarding wave-energy absorption are found to converge toward varying irregular patterns, depending on the number of rows and on the values of the input parameters $\{r, t, d\}$. However, these optimal configurations show limited improvements over regular arrays of $l = \lambda/4$, with maximal differences appearing for low dissipation values. This model also shows a negligible impact of array interference on wave transmission, which would depend mainly on array size and on local parameters. This is seen to arise from a competition between reflection and damping, with large oscillations compensating for a low global reflection and vice versa. It should, however, be noted that the simple model may not be sufficient to account for drag effects, which could potentially lead to larger variations of the transmission coefficients. In terms of WEC-farm design, the results presented here suggest that array configurations can indeed help improve energy harvesting but will be limited in their impact on wave transmission. A more-effective solution for the latter would be to seek means of reducing local transmission coefficients.

ACKNOWLEDGMENTS

We acknowledge support from the INSIS-CNRS PEPS et Réseaux "Ingénierie verte" 2018 program through the project "Bio-inspired wave-energy absorbers." We are also grateful to the Manipulation d'Ondes de Surface team in the Laboratoire de Physique et Mécanique des Milieux Hétérogènes for their valuable help and support.

APPENDIX: DERIVATION OF R_N AND T_N

The general expressions for R_n and T_n given in Eq. (9) are derived here, starting with a simple case of only two rows.

1. Two-row case

Taking the case of an array composed of two rows only, we have

$$\mathcal{A}_1 = |T_1 - R_1| = |1 - R_1|, \tag{A1}$$

$$\mathcal{A}_2 = |T_2 - R_2| = |T_2|. \tag{A2}$$

Developing the reflection factor R_1 of row 2 acting on row 1 with multiple reflections gives

$$\begin{aligned} R_1 &= rte^{i(2\varphi)} + r^3te^{i(4\varphi)} + \cdot s + r^nte^{i[(n+1)\varphi]}, \\ &= tre^{i2\varphi}\sum_{k=0}^{N} r^{2n}e^{i2n\varphi} = tre^{i2\varphi}\frac{1-(r^2e^{i2\varphi})^n}{1-r^2e^{i2\varphi}}, \\ R_1 &= \frac{tre^{i2\varphi}}{1-r^2e^{i2\varphi}}. \end{aligned} \tag{A3}$$

Developing the transmission factor T_2 of row 1 acting on row 2 with multiple reflections gives

$$\begin{aligned} T_2 &= te^{i(\varphi)} + r^2te^{i(3\varphi)} + \cdot s + r^nte^{i[(n+1)\varphi]}, \\ &= te^{i\varphi}\sum_{n=0}^{N} r^{2n}e^{i2n\varphi} = te^{i\varphi}\frac{1-(r^2e^{i2\varphi})^n}{1-r^2e^{i2\varphi}}, \\ T_2 &= \frac{te^{i\varphi}}{1-r^2e^{i2\varphi}}. \end{aligned} \tag{A4}$$

Substituting Eqs. (A3) and (A4) into Eqs. (A1) and (A2), we now have

$$\mathcal{A}_1 = \left|1 - \frac{tre^{i2\varphi}}{1-r^2e^{i2\varphi}}\right|, \tag{A5}$$

$$\mathcal{A}_2 = \left|\frac{te^{i\varphi}}{1-r^2e^{i2\varphi}}\right|. \tag{A6}$$

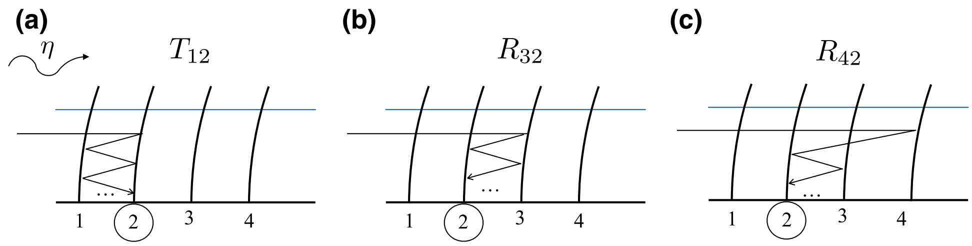

FIG. 10. Example of the considered multiple reflections taken into account for the calculation of R_n and T_n applied to the case of row 2 in a four-row array. Illustrations of the transmitted waves (a), reflected waves from row 3 (b), and reflected waves from row 4 (c).

2. Generalization

We now wish to generalize these sets of equations to a number N of rows in order to perform a global analysis of the array interference based on local mechanisms. For multiple reflections within the array, the total number of reflected terms increases very rapidly with the number of rows N, leading to very complex formulations. For example, if we take into account the first two terms only of all possible multiple reflections, row $n+1$ contributes two reflection terms, row $n+2$ contributes four terms, row $n+3$ contributes seven terms, and so on. Therefore, the number of added terms per row follows an arithmetic series with increasing common difference n due to the increasing number of combinations of intermediate reflections. However, the coefficients r and t are both $\mathcal{O}(10^{-1})$, and so the terms of high-order reflections reduce rapidly, and can be ignored.

Terms arising from multiple reflections between two non-neighboring rows decrease by a factor of at least r^2t^2, corresponding to $\mathcal{O}(10^{-4})$, which leads to an infinite sum factor $[1-(r^2t^2)^{N+1}]/(1-r^2t^2) \approx 1$, where N represents the total number of reflections. These terms therefore do not influence the first term of the sum and can be ignored. Multiple reflections are thus limited to the immediate neighbors only. For example, in a system consisting of four rows, the infinite reflections of waves reaching row 2 will be considered between row 2 and row 3 only, regardless of the source of emission, as shown in Fig. 10 for the case of a four-row array. The same holds for the transmission-coefficient term.

Developing the expressions for the amplification-factor calculation on row 2 gives the following:

$$T_{12} = \frac{te^{i(\varphi_1+\varphi_2)}}{1-r^2e^{i2\varphi_2}}, \tag{A7}$$

$$R_{32} = \frac{rt^2e^{i(\varphi_1+\varphi_2+2\varphi_3)}}{1-r^2e^{i2\varphi_3}} = \frac{rt^2e^{i(\varphi_1+\varphi_2)}\times t^0e^{i2\varphi_3}}{1-r^2e^{i2\varphi_3}}, \tag{A8}$$

$$R_{42} = \frac{rt^4e^{i[\varphi_1+\varphi_2+2(\varphi_3+\varphi_4)]}}{1-r^2e^{i2\varphi_3}} = \frac{rt^2e^{i(\varphi_1+\varphi_2)}\times t^2e^{i2(\varphi_3+\varphi_4)}}{1-r^2e^{i2\varphi_3}}. \tag{A9}$$

Each subsequent row (rows 3 and 4 in this case) will reflect waves that are themselves infinitely reflected locally to row 2, as represented in the denominator of both R_n terms [Eqs. (A8) and (A9)]. A pattern is therefore identified in the total reflection term, with a second geometric series corresponding to the additional reflections caused by subsequent rows. The generalized equations for any row n can then be written from the sums of these combined geometric series as follows [Eq. (9)]:

$$R_n = \underbrace{\frac{rt^ne^{i[\sum_{m=1}^{n}\varphi_m]}}{1-r^2e^{i2\varphi(n+1)}}}_{\text{immediate neighbors}} \underbrace{\sum_{k=0}^{N-n-1} t^{2k}e^{i2\sum_{m=n+1}^{k+n+1}\varphi_m}}_{\text{subsequent rows}},$$

$$T_n = \frac{t^{(n-1)}e^{i\sum_{m=1}^{n}\varphi_m}}{1-r^2e^{i2\varphi_n}}.$$

[1] B. Drew, A. R. Plummer, and M. N. Sahinkaya, in *Proceedings of the Institution of Mechanical Engineers, Part A: Journal of Power and Energy* (Sage Publications Sage UK: London, England, 2009), Vol. 223.

[2] A. Clément, P. McCullen, A. Falcão, A. Fiorentino, F. Gardner, K. Hammarlund, G. Lemonis, T. Lewis, K. Nielsen, and S. Petroncini et al., Wave energy in Europe: Current status and perspectives, Renewable Sustainable Energy Rev. **6**, 405 (2002).

[3] J. Falnes, *Ocean waves and oscillating systems: Linear interactions including wave-energy extraction* (Cambridge University Press, Cambridge, 2002).

[4] A. Day, A. Babarit, A. Fontaine, Y.-P. He, M. Kraskowski, M. Murai, I. Penesis, F. Salvatore, and H.-K. Shin, Hydrodynamic modelling of marine renewable energy devices: A state of the art review, Ocean Eng. **108**, 46 (2015).

[5] F. Dias, E. Renzi, S. Gallagher, D. Sarkar, Y. Wei, T. Abadie, C. Cummins, and A. Rafiee, Analytical and computational modelling for wave energy systems: The example of oscillating wave surge converters, Acta Mech. Sin. **1**, 647 (2017).

[6] A. Babarit, On the park effect in arrays of oscillating wave energy converters, Renewable Energy **58**, 68 (2013).

[7] B. Borgarino, A. Babarit, and P. Ferrant, Impact of wave interactions effects on energy absorption in large arrays of wave energy converters, Ocean Eng. **41**, 79 (2012).

[8] D. Sarkar, E. Renzi, and F. Dias, in *Proceedings of the Royal Society A* (The Royal Society, London, 2014), Vol. 470, p. 20140118.
[9] D. Sarkar, K. Doherty, and F. Dias, The modular concept of the oscillating wave surge converter, Renewable Energy **85**, 484 (2016).
[10] Y. Wei, T. Abadie, A. Henry, and F. Dias, Wave interaction with an oscillating wave surge converter. Part II: Slamming, Ocean Eng. **113**, 319 (2016).
[11] G. Arnaud, V. Rey, J. Touboul, D. Sous, B. Molin, and F. Gouaud, Wave propagation through dense vertical cylinder arrays: Interference process and specific surface effects on damping, Appl. Ocean Res. **65**, 229 (2017).
[12] N. Kaina, M. Fink, and G. Lerosey, Composite media mixing Bragg and local resonances for highly attenuating and broad bandgaps, Sci. Rep. **3**, 3240 (2013).
[13] A. Colombi, P. Roux, S. Guenneau, P. Gueguen, and R. V. Craster, Forests as a natural seismic metamaterial: Rayleigh wave bandgaps induced by local resonances, Sci. Rep. **6**, 19238 (2016).
[14] S. Brûlé, E. Javelaud, S. Enoch, and S. Guenneau, Experiments on Seismic Metamaterials: Molding Surface Waves, Phys. Rev. Lett. **112**, 133901 (2014).
[15] M. Miniaci, A. Krushynska, F. Bosia, and N. M. Pugno, Large scale mechanical metamaterials as seismic shields, New J. Phys. **18**, 083041 (2016).
[16] B. Sharma, and C.-T. Sun, Local resonance and Bragg bandgaps in sandwich beams containing periodically inserted resonators, J. Sound Vibration **364**, 133 (2016).
[17] X. Hu, and C. Chan, Refraction of Water Waves by Periodic Cylinder Arrays, Phys. Rev. Lett. **95**, 154501 (2005).
[18] J. Abanades, D. Greaves, and G. Iglesias, Coastal defence using wave farms: The role of farm-to-coast distance, Renewable Energy **75**, 572 (2015).
[19] E. Guazzelli, V. Rey, and M. Belzons, Higher-order Bragg reflection of gravity surface waves by periodic beds, J. Fluid. Mech. **245**, 301 (1992).
[20] L.-A. Couston, M. A. Jalali, and M.-R. Alam, Shore protection by oblique seabed bars, J. Fluid. Mech. **815**, 481 (2017).
[21] C. Nové-Josserand, F. C. Hebrero, L. Petit, W. Megill, R. GodoyDiana, and B. Thiria, Surface wave energy absorption by a partially submerged bio-inspired canopy, Bioinspir. Biomim. **13**, 036006 (2018).
[22] X. Garnaud, and C. C. Mei, in Proceedings of the Royal Society of London A:Mathematical, Physical and Engineering Sciences (The Royal Society, London, 2009), p. rspa20090458.
[23] E. Renzi, and F. Dias, Relations for a periodic array off lap-type wave energy converters, Appl. Ocean Res. **39**, 31 (2013).
[24] M. Göteman, J. Engström, M. Eriksson, and J. Isberg, Optimizing wave energy parks with over 1000 interacting point-absorbers using an approximate analytical method, Int. J. Marine Energy **10**, 113 (2015).
[25] F. Moisy, M. Rabaud, and K. Salsac, A synthetic schlieren method for the measurement of the topography of a liquid interface, Exp. Fluids **46**, 1021 (2009).